Vol. 25, No. 1(2026) Sim26720

Revista Mexicana de Ingeniería Química

Numerical-experimental study of a solar dryer using Computational Fluid Dynamics (CFD) for its optimization

Estudio numérico-experimental de un Secador Solar mediante la Dinámica de Fluidos Computacional (CFD) para su optimización

A. Tlatelpa-Becerro[1]*, L. Castro[2], M. Rebolledo Abri[2], I.S. Avilés-López[1], M. Navarrete-Procopio[3], V.M. Zezatti-Flores[2], E. O. Castañeda Magadán[3]

[1]Robotic Engineering Department, Escuela de Estudios Superiores de Yecapixtla, Universidad Autónoma del Estado de Morelos, Yecapixtla Morelos 62824, México

[2]Centro de Investigación en Ingeniería y Ciencias Aplicadas, Universidad Autónoma del Estado de Morelos, Cuernavaca, 62209, México

[3]Facultad de Ciencias Químicas e Ingeniería, Universidad Autónoma del Estado de Morelos, Cuernavaca Morelos 62209, México

Received: November 19, 2025; Accepted: January 19, 2026

Abstract

This research work involved a numerical-experimental study of a forced-flow, indirect solar dryer using computational fluid dynamics (CFD) for optimization. The dryer has two main parts: a drying chamber that captures radiant energy from the sun, through which airflow is passed to increase its temperature before being transported to the drying chamber, where the products are dried. The dryer was instrumented with temperature sensors to record the data, which were used in the computational modeling. The computational simulations predicted that reducing the height of the drying chamber to 50 cm would increase the average temperature to 13.43 K compared to the original design. Therefore, CFD is a powerful tool for studying solar dryers, offering both technical and economic advantages.

Keywords: Solar dryer, Computational Fluid Dynamics, Optimization.

Resumen

Este trabajo de investigación consistió en un estudio numérico-experimental de un secador solar indirecto de flujo forzado mediante dinámica de fluidos computacional (CFD) para su optimización. El secador consta de dos partes principales: una cámara de secado que capta la energía radiante del sol, a través de la cual se hace pasar el flujo de aire para aumentar su temperatura antes de ser transportado a la cámara de secado, donde se secan los productos. El secador se instrumentó con sensores de temperatura para registrar los datos, que se utilizaron en el modelado computacional. Las simulaciones computacionales predijeron que reducir la altura de la cámara de secado a 50 cm aumentaría la temperatura promedio a 13,43 K en comparación con el diseño original. Por lo tanto, la CFD es una herramienta poderosa para el estudio de secadores solares, que ofrece ventajas tanto técnicas como económicas.

Palabras clave: Secador solar, Dinámica de Fluidos Computacional, Optimización.

* *Corresponding author. E-mail*: angel.tlatelpa@uaem.mx ;
https://doi.org/10.24275/rmiq/Sim26720
ISSN:1665-2738, *issn-e*: 2395-8472

1 Introduction

Energy demand has been increasing, exceeding the capacity of conventional sources to meet it sustainably. It is due to population growth, urban expansion, and industrial progress. In this scenario, the use of renewable energy is essential to reduce dependence on fossil fuels and mitigate the consequences of climate change. Due to its advantageous geographic location, Mexico has significant potential for solar energy, with a daily average of 5.5 $\frac{kWh}{m^2}$ (Government of Mexico, 2016; Limón Portillo, 2017). Despite this, this resource remains largely untapped, especially in the agro-industrial sector.

Today, the greatest opportunity for solar energy's significant impact lies in the food drying process, which accounts for 20%-30% of energy consumption in the agricultural industry (Cetina-Quiñoñnes *et al*., 2021). Despite this, conventional drying methods are still used, which entail high operating costs and a significant environmental impact due to the need for heating mechanisms, whether through traditional fuels such as hydrocarbons or natural gas, or electricity generated by coal-fired power plants. In this sense, to mitigate greenhouse gas emissions and energy consumption from non-renewable energy sources, solar energy is the ideal option (García-Moreira *et al*., 2024).

Regarding the use of solar energy in solar dryers, these are a good alternative. These devices capture the sun's radiant energy and transform it into thermal energy (Figueroa-García *et al*., 2021). This energy is transferred to an airflow entering the solar collector through natural or forced convection (Kebede *et al*., 2024), increasing its temperature and directing it toward a drying chamber where the products to be dried are placed. This process removes the water content from products such as fruits, vegetables, herbs, grains, and meats. In this process, drying is expected to be essential for food preservation and for reducing post-harvest losses, thereby extending shelf life (García-Moreira *et al*., 2025).

On the other hand, direct solar drying, while economical, presents risks of product contamination and quality loss (Doymaz & Ísmail, 2011). However, technological advances in solar drying equipment have evolved significantly, making it a promising and viable alternative in the food drying sector.

Therefore, at the Yecapixtla Higher School of Studies (EESY), an indirect forced-flow solar dryer has been installed to dehydrate meats, fruits, and vegetables. This equipment, consisting of a solar collector and a drying chamber, harnesses solar radiation to heat the air circulating through the system. However, to ensure its efficiency and viability as a sustainable alternative, it is necessary to understand and optimize its thermal performance under different environmental conditions.

Numerical simulation using Computational Fluid Dynamics (CFD) offers a powerful tool for analyzing heat transfer phenomena in solar dryers, eliminating the need to build multiple physical prototypes. However, for simulation results to be reliable, it is essential to validate the model using field experimental data. (Demissie *et al*., 2019) (Romero *et al*., 2014). This tool has also been helpful in other case studies, where it models transient heat transfer and compares results with the lumped capacitance modeling technique, enabling the modeling and prediction of heat transfer phenomena at temperatures above 40 °C (Tegenaw *et al*., 2019).

The main problem is that, while the indirect solar dryer installed at the EESY (Yucatán Experimental Station) meets the basic operating principles, no detailed study has been conducted to optimize its design and operation. This study encompasses the system's geometry, the materials used, the boundary conditions, and the applied turbulence model. It is also necessary to evaluate proposed improvements, such as increasing the drying chamber size, to improve the system's thermal efficiency. For this purpose, Computational Fluid Dynamics (CFD) was used with Ansys Fluent.

2 Materials and methods

The study was divided into two stages: data collection and numerical analysis. Both were used to validate the thermal behavior of the indirect solar dryer and to propose design improvements using computational fluid dynamics.

2.1 Experimental indirect solar dryer

The drying system used was an indirect, forced-flow solar dryer installed at the Yecapixtla Higher Education School (18.853° N, 98.869° W), where the experiment was conducted. This equipment consists of two main parts, as described below and shown in Figure 1a:

- Solar collector: Solar collector: Designed to capture solar radiation and transfer heat to the air circulating inside. It is constructed from a stainless-steel casing and features fiberglass insulation between the casing and a flat aluminum plate that reflects energy toward the pipes. It contains 16 copper pipes, each 1.5 meters long, with an external diameter of 2.66 cm and a schedule of 0.01 cm. These pipes are painted matte black to maximize solar radiation absorption during the day and increase the tem-

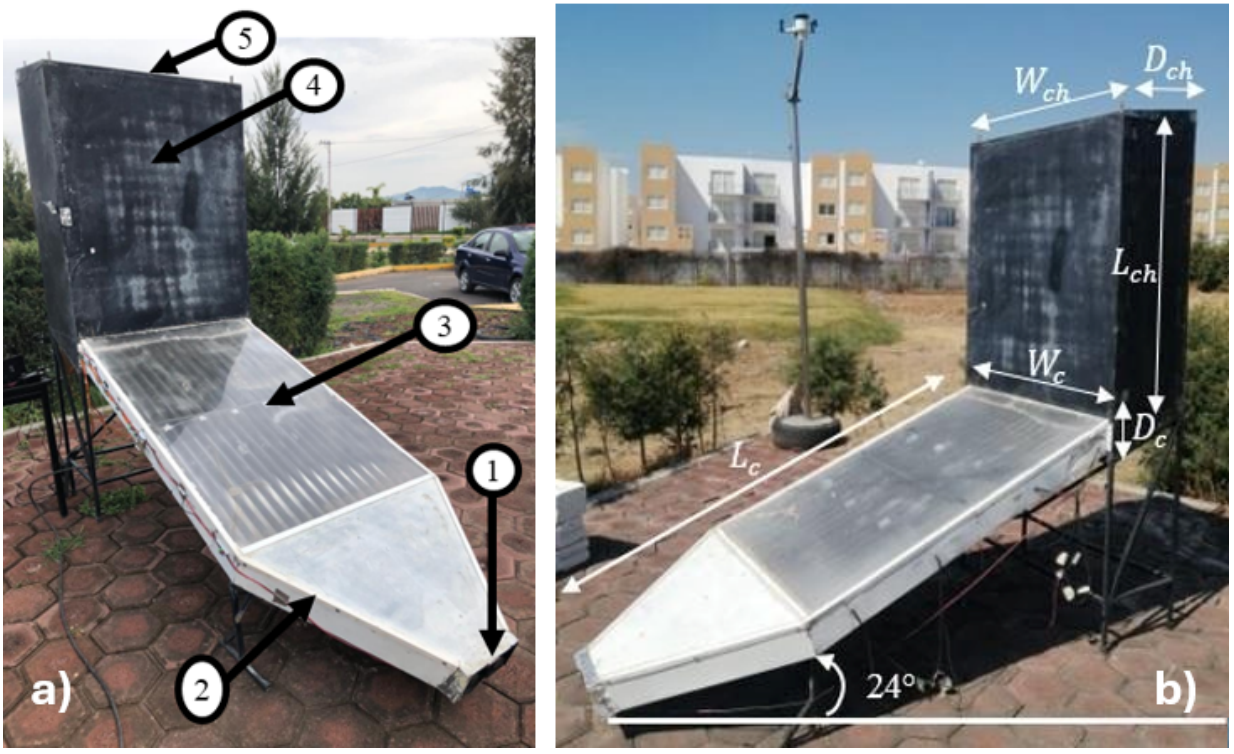

Figure 1. a) Parts of the solar dryer, where: (1) dryer inlet, (2) stainless steel casing, (3) solar collector, (4) drying chamber, (5) dryer outlet. b) Dimensions of the solar dryer. b) Dimensions of the experimental solar dryer.

perature of the air entering the drying chamber.

- Drying chamber: Made of stainless steel and painted matte black to capture maximum solar radiation. An air outlet with a diameter of 2.54 cm is located at the top front. The chamber has a capacity of 15 trays, each for drying products.

The dimensions of the collector are as follows: length of (L_c) 2.145 m, width of (W_c) 0.95 m, and height of (D_c) of 0.13 m; and for the chamber: height of (L_{ch}) 1.27 m, width of (W_{ch}) 1.01 m, and depth of (D_{ch}) 0.455 m, see Figure 1b. The equipment was positioned facing south to maximize solar radiation during the experiment.

2.2 *Electronic instrumentation*

An instrumentation system was implemented to enable the acquisition of the most relevant experimental data. For this, seven K thermocouple types were installed to monitor temperatures in pipes 3, 6, 9, 11, and 15 of the solar collector, at the positions shown in Figure 2a. At the entrance to the solar collector, two NMB-brand fans were installed, operating at 12 volts and 1.3 amps, with a flow rate of 1.4 $\frac{m}{s}$. To measure the airflow speed, two anemometers were installed: one on the solar collector (model Ut363, with a resolution of 0.1 m/s) and a second one on the upper front of the drying chamber (model her-440, with a resolution of 0.01 m/s), as shown in Figures 2a and 2c, respectively. Three DHT22 humidity and temperature sensors were installed inside the drying chamber, centered and vertically oriented (Figure 2d). The temperature and humidity sensors were connected to a data acquisition board (Arduino, Monza, Italy), while the airflow velocity was measured manually. All data was recorded and stored for processing.

2.3 *Computational modeling*

Using geometric data, a three-dimensional model of the solar dryer was created using a parametric computer-aided design (CAD) program. This CAD tool allowed the generation of precise system geometry for subsequent numerical analysis, including internal volumes, air inlets and outlets, and thermal contact surfaces.

The next step is to perform numerical analysis using a CFD simulation program to solve the governing Navier-Stokes equations, which conserve mass, momentum, and energy (Bird *et al*., 2006; Getahun *et al*., 2021).

$$\frac{\partial \rho}{\partial t} + \nabla \cdot (\rho \mathbf{u}) = 0 \tag{1}$$

$$\frac{\partial (\rho \mathbf{u})}{\partial t} + \nabla \cdot (\rho \mathbf{u}\mathbf{u}) = -\nabla P - \nabla \cdot \boldsymbol{\tau} + \rho \mathbf{g} \tag{2}$$

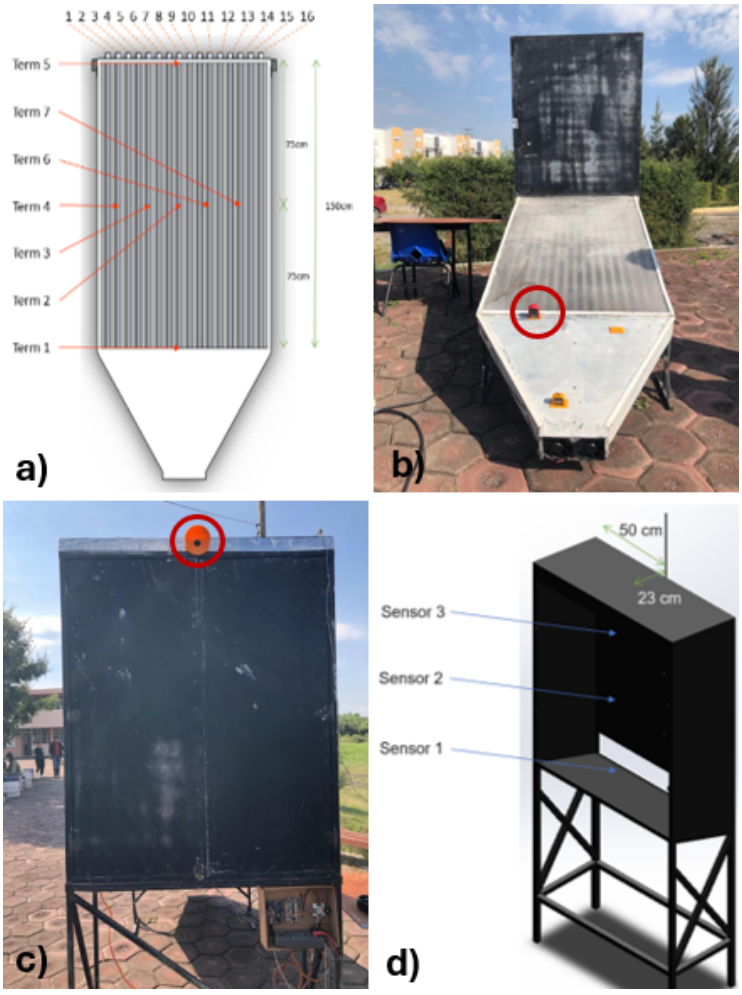

Figure 2. a) Location of type K sensors on the solar collector. b) Location of the anemometer on the solar collector. c) Location of the anemometer in the drying chamber. d) Position of the DHT22 sensors.

$$\frac{\partial(\rho E)}{\partial t} + \nabla \cdot (\mathbf{u}(\rho E + P)) = \nabla \cdot (-\mathbf{q}) + \boldsymbol{\tau} : \nabla \mathbf{u} + S_h \quad (3)$$

The continuity equation (1) is derived from the law of conservation of mass and describes the rate of change of fluid density with respect to time at a fixed point in space.

To obtain the equation of motion (2), a momentum balance is performed on a volume element. The term $\frac{\partial(\rho \mathbf{u})}{\partial t}$ represents the rate of momentum increase per unit volume, $\nabla \cdot (\rho \mathbf{uu})$ indicates the rate of momentum addition by convection per unit volume, the terms $-\nabla P - \nabla \cdot \boldsymbol{\tau}$ represent the rate of momentum addition by molecular transport per unit volume, and $\rho \mathbf{g}$ represents the gravitational force on the fluid per unit volume. The energy equation (3) is derived from the first law of thermodynamics, which states that energy is conserved. The internal energy plus the kinetic energy plus the time increase of the internal energy plus the kinetic energy within the control volume must equal the work done on the control volume by both volumetric and surface forces (Xamán & Gijón-Rievera, 2016). The total energy is the sum of the internal energy and the kinetic energy, and is given by:

$$E = h - \frac{P}{\rho} + \frac{u^2}{2} \quad (4)$$

The study continued with a mesh configuration for the CFD model, refining critical areas such as the air inlet, collector pipes, and drying chamber to model airflow and temperature distribution within the equipment. A mesh independence analysis was performed using the mesh convergence index (GCI), with an error of less than 10% (equation 5; Galindo Luna *et al*., 2017), thereby ensuring the reliability of the results.

$$GCI = \frac{3|\varepsilon|}{r^{P-1}} \quad (5)$$

During processing, the RNG $\kappa - \varepsilon$ model was selected, which offers better accuracy in flows with recirculation and curvatures (Afshari *et al*., 2021; Benhamza *et al*., 2021; Güler *et al*., 2020), such as those present in the solar collector.

Table 1. Boundary conditions used in the computer simulations.

Part of the dryer	**Boundary condition type**	**Thermal condition**
Drying chamber Housing Acrylic Tubes	Wall	System coupling
Tube inlet	Inside	N/A
Dryer entry and exit boundary condition	**Inlet**	**Oulet**
Boundary condition type	Velocity input	Velocity oulet
Turbulence intensity (%)	5.00	5.00
Hydraulic diameter (m)	0.12	0.0254

Table 2. Results in the GCI analysis process in CFD.

Mesh number	Element size (m)	(T_{cs}) (K)	GCI (%)
1	0.130	320.924	N/A
2	0.095	318.323	2.809
3	0.070	317.422	1.012

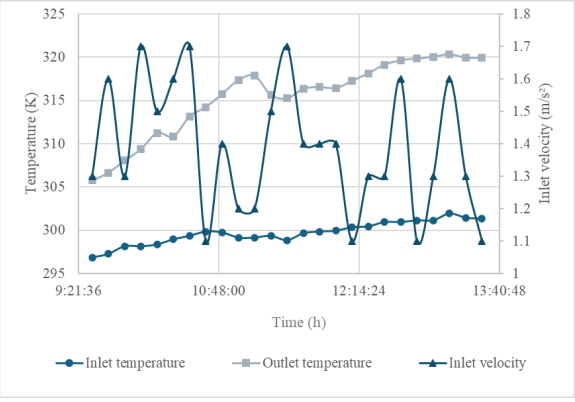

Figure 3. Experimental data used in boundary conditions.

For the boundary conditions, an air inlet velocity was established based on experimental measurements (see Table 1). Also, actual field-measured temperatures on the collector and chamber walls were applied, while the air outlet was defined under normal atmospheric conditions in the area (Figure 3). The air was modeled as a compressible fluid with temperature-dependent properties, enabling a more realistic simulation of its thermal behavior.

All the data considered allowed us to establish the boundary conditions in the computational fluid dynamics (CFD) simulations. To this end, 25 simulations were performed at different times of day between 9:30 a.m. and 1:30 p.m. Although transient behavior was not modeled in this case study, the steady-state approach yielded a representative thermal profile of the system with good results. In the post-processing stage, 4000 iterations were performed, resulting in stable residuals, indicating that the conservation conditions were met. However, while there are related studies of transient solar air heaters using CFD (Elakrout *et al.*, 2025), these serve as a basis for future work in our research to model heat transfer.

3 Results and discussion

The experiment was conducted on October 14, 2022, from 9:30 a.m. to 1:30 p.m., with 10-minute intervals between each measurement. The same set of boundary conditions was maintained throughout the simulations, with only the experimental data varying at each time interval. The results were examined using the Ansys Fluent CFD-Post tool, which showed temperature profiles of the copper tubes in the solar collector and the drying chamber.

3.1 Mesh convergence

In CFD simulations, properly discretizing the physical domain into a mesh is crucial for solving the conservation equations of mass, momentum, and energy, as an inadequate mesh can introduce significant numerical errors. To avoid these errors, a mesh independence analysis, or grid convergence index (GCI), is performed to quantify the relative error between solutions obtained with different mesh sizes.

To perform the GCI, steady-state simulations of the solar dryer were conducted at 1:30 p.m., using three mesh configurations with different element sizes in the drying chamber:

- Mesh 1 (coarse): element size of 0.130 m
- Mesh 2 (medium): element size of 0.095 m
- Mesh 3 (fine): element size of 0.070 m

The temperature in the drying chamber (T_{cs}), was used as a comparison parameter because it is critical to evaluating the system's thermal performance. The results obtained are presented in Table 2, which reports the simulated temperatures and the corresponding GCI values.

According to Galindo Luna *et al*. (2017), a GCI value below 10% is considered acceptable to ensure mesh independence. In this case, models 2 and 3 meet this criterion, with mesh 3 exhibiting the lowest GCI (1.012%), indicating greater accuracy and allowing better resolution of the thermal and velocity gradients within the solar dryer.

The temperature difference between the coarse (320.924 K) and fine (317.422 K) meshes is approximately 3.5 K, corresponding to a 1.09% variation. This difference can be significant in applications where thermal control is essential, such as food drying, where variations of just a few degrees can affect the quality of the final product.

3.2 Heat transfer

One of the most critical aspects of thermal analysis in a solar drying system is quantifying heat transfer. It allows for the evaluation of the solar collector's efficiency and its ability to raise the temperature of the air circulating into the drying chamber.

The calculations are based on the methodology proposed by Castañeda Magadán (2017), using the air temperatures and velocities measured during the experimental tests. To determine the thermodynamic properties of air (density, heat capacity, thermal conductivity, and dynamic and kinematic viscosity), thermodynamic tables (Cengel & Ghajar, 2011) were used. When exact data for certain temperatures were unavailable, linear interpolation was used to estimate specific operating values for the dryer. Using the air velocity measured by the anemometers installed on the equipment and the calculated air density, the mass flow rate (m) was calculated using equation 6; and to determine the volumetric flow rate, the mass flow rate was divided by the air density.

$$\dot{m} = \rho \cdot A \cdot V \tag{6}$$

where:

- ρ: air density $\left(\frac{kg}{m^3}\right)$.
- A: cross-sectional area of the duct.
- V: air velocity.

Next, the Reynolds number (Re) was calculated to determine the flow regime within the solar collector, using the hydraulic diameter (D_h) (Cengel & Ghajar, 2011) as a geometric parameter, given that the flow occurs in circular tubes:

$$Re = \frac{\rho \cdot V \cdot D_h}{\mu} \tag{7}$$

The Reynolds number values obtained confirmed that the flow was turbulent, validating the use of the RNG $\kappa - \varepsilon$ turbulence model in CFD simulations.

3.2.1 Nusselt number and convective coefficient

The Nusselt number (Nu) is a dimensionless parameter that summarizes the efficiency of convective heat transfer relative to conduction. This number allows us to evaluate the effectiveness of heat transfer from the tube to the air inside and to compare different designs or conditions without the need for physical units.

For this study, Nu was calculated using Zukauskas's (1972) evaluation for crossflows over tube arrangements.

$$Nu = 0.27 \cdot Re^{0.63} \cdot Pr^{0.36} \cdot \left(\frac{\mathrm{Pr}}{Pr_w}\right)^{0.25} \tag{8}$$

With this value of Nu and the thermal conductivity of the fluid (k), the convective heat transfer coefficient (h) was determined.

$$h = \frac{Nu \cdot k}{D_h} \tag{9}$$

3.2.2 Heat transfer rate

Finally, the heat transfer rate (Q) was calculated using.

$$Q = h \cdot A \cdot (T_s - T_\infty) \tag{10}$$

where:

- T_s: tube surface temperature
- T_∞: inlet air temperature

These calculations allowed us to estimate the amount of thermal energy transferred to the air, which is fundamental for evaluating the solar collector's efficiency (Table 3). The results showed good agreement with the CFD model, with a relative percentage error below 5% between the experimental $\left(T_{exp,\,tub}\right)$ and simulated ($T_{sim,\,tub}$) temperatures. The error was calculated to quantify the difference between the experimental and simulated values , as shown in equation 11 (Iranmanesh, Hadi, & Saleh, 2020).

$$E_r(\%) = \left|\frac{Value_{experimental} - Value_{simulated}}{Value_{experimental}}\right| \times 100 \tag{11}$$

Table 3. Comparison of pipe temperatures between experimental and simulated tests.

No. thermocouple	Time (h)	($T_{exp,tub}$) (K)	($T_{sim,tub}$) (k)	E_r (%)
	09:30:00	301.65	307.98	2.1
1	11:30:00	308.15	307.07	0.35
	01:30:00	310.9	316.87	1.92
	09:30:00	311.9	318.38	2.08
2	11:30:00	326.15	316.95	2.82
	01:30:00	330.15	326.25	1.18
	09:30:00	311.4	318.23	2.19
3	11:30:00	325.15	316.84	2.56
	01:30:00	330.9	326.01	1.48
	09:30:00	311.15	319.33	2.63
4	11:30:00	325.15	317.83	2.25
	01:30:00	328.15	327.01	0.35
	09:30:00	306.15	321.4	4.98
5	11:30:00	321.65	314.2	2.32
	01:30:00	325.4	328.47	0.94
	09:30:00	310.4	318.72	2.68
6	11:30:00	325.4	317.21	2.52
	01:30:00	331.4	326.08	1.61
	09:30:00	313.9	319.58	1.81
7	11:30:00	330.15	317.78	3.75
	01:30:00	337.4	327.42	2.96

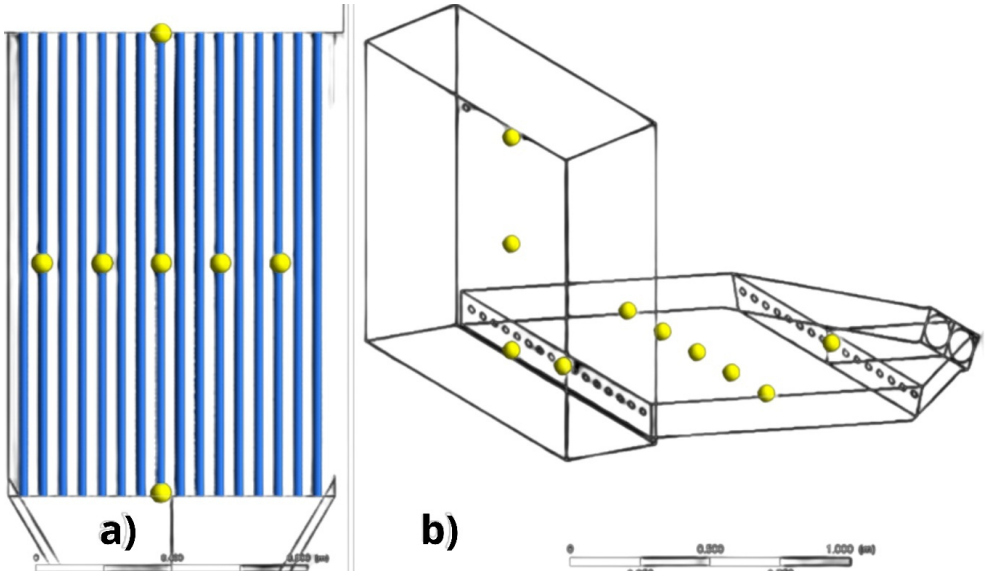

Figure 4 Temperature measurement points in a) copper pipe and b) drying chamber.

3.3 CFD model validation

Seven type K thermocouples were installed in the copper pipes of the solar collector, and three DHT22 sensors in the drying chamber. These points were replicated in the CFD model to obtain simulated temperatures at the exact real locations; see Figure 4.

Figure 5 shows the temperature contours for the solar dryer at three times of day. As shown, the air entering the solar collector at ambient temperature gradually increases in temperature as it passes through the tubes, reaching its maximum temperature upon entering the drying chamber. The inlet velocities to the solar dryer were 1.30, 1.70, and 1.10 $\frac{m}{s}$, for 9:30 a.m., 11:30 a.m., and 1:30 p.m., respectively. Furthermore, the solar dryer reaches a higher temperature at 1:30 p.m. than at the other two times. It is due to a lower flow rate in the pipe, which keeps the warm air in contact with the walls of the solar collector tubes for a longer period.

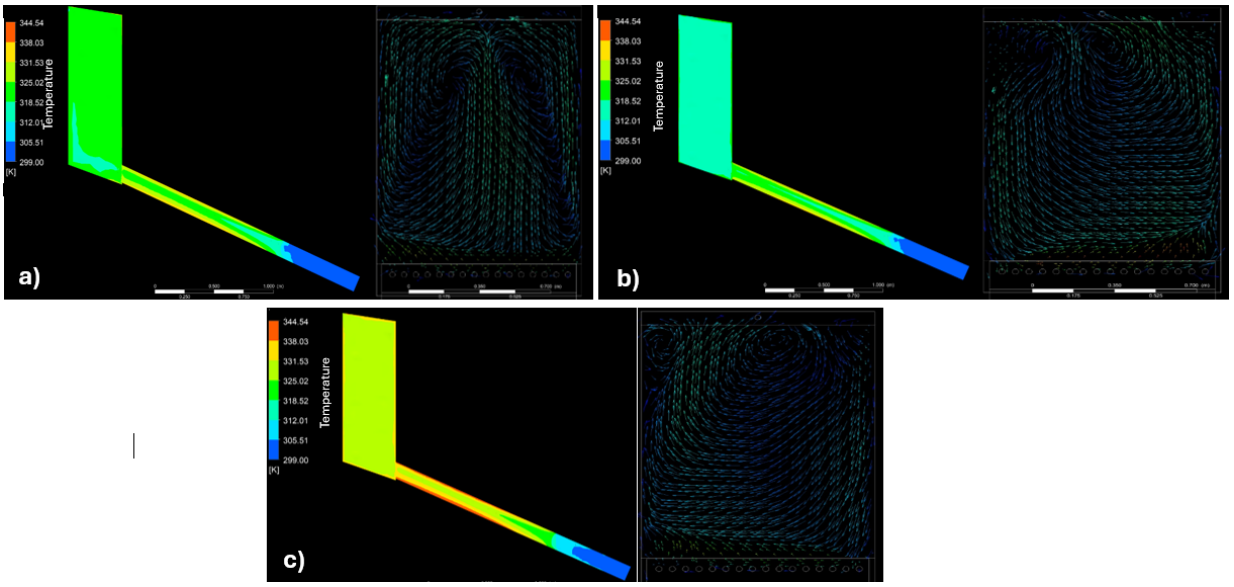

Figure 5. Side view of the temperature contour of the model for the times of: a) 09:30 h. b) 11:30 h c) 13:30 h.

Table 4. Comparison of pipe temperatures between experimental and simulated tests.

No. thermocouple	**Time (h)**	$(T_{exp,tub})$ (K)	$(T_{sim,tub})$ (K)	Er (%)
	09:30	301.65	307.98	2.10
1	11:30	308.15	307.07	0.35
	13:30	310.90	316.87	1.92
	09:30	311.90	318.38	2.08
2	11:30	326.15	316.95	2.82
	13:30	330.15	326.25	1.18
	09:30	311.40	318.23	2.19
3	11:30	325.15	316.84	2.56
	13:30	330.90	326.01	1.48
	09:30	311.15	319.33	2.63
4	11:30	325.15	317.83	2.25
	13:30	328.15	327.01	0.35
	09:30	306.15	321.40	4.98
5	11:30	321.65	314.20	2.32
	13:30	325.40	328.47	0.94
	09:30	310.40	318.72	2.68
6	11:30	325.40	317.21	2.52
	13:30	331.40	326.08	1.61
	09:30	313.90	319.58	1.81
7	11:30	330.15	317.78	3.75
	13:30	337.40	327.42	2.96

Figure 5 shows the temperature contours of the solar dryer at three different times of day. As shown, the air entering the solar collector at ambient temperature gradually increases in temperature as it passes through the tubes, reaching its maximum temperature upon entering the drying chamber. The solar radiation and inlet velocities used for the solar dryer were 517 $\frac{W}{m^2}$, 1.30 $\frac{m}{s}$; 773 $\frac{W}{m^2}$, 1.70 $\frac{m}{s}$ and 787 $\frac{W}{m^2}$, 1.10 $\frac{m}{s}$ at 9:30, 11:30, and 13:30, respectively. These three times of day were considered because they represent the minimum, intermediate, and maximum values (Figure 3) to understand the thermal behavior at these times. The highest temperature was recorded at 13:30, approximately 338 K. This is due to a lower flow rate in the pipe, which keeps the hot air in contact with the walls of the solar collector tubes for a more extended period, and to better airflow circulation within the chamber. Considering the radiation was 14 W/m^2 higher than at 11:30.

For model verification, Table 4 compares the CFD-simulated temperatures $(T_{sim,\,tub})$ with the experimental temperatures $\left(T_{exp,\,tub}\right)$ of the pipes.

Table 5. Comparison of experimental versus simulated temperature in the sensors of the drying chamber.

No. DHT22 sensor	Time (h)	$(T_{exp,cs})$ (K)	$(T_{sim,cs})$ (K)	E_r (%)
1	09:30:00	305.25	318.88	4.46
	11:30:00	315.05	315.1	0.02
	01:30:00	319.15	327.95	2.76
2	09:30:00	305.65	318.68	4.26
	11:30:00	315.65	315.09	0.18
	01:30:00	319.25	328.02	2.75
3	09:30:00	305.75	318.7	4.24
	11:30:00	315.25	315.35	0.03
	01:30:00	319.95	328.44	2.65

Table 6. Comparison of temperatures inside the drying chamber at different heights.

$(T_{exp,cs})$	$(T_{sim,cs})$	$T_{sim,cs}$ 100 cm	$T_{sim,cs}$ 80 cm	$T_{sim,cs}$ 50 cm
319.45	328.13	330.43	336.71	342.13

The maximum calculated relative percentage error ($E_r(\%)$) was 4.98% and the minimum was 0.35%.

On the other hand, Table 5 shows the comparison of the experimental temperatures$\left(T_{exp,cs}\right)$ with the simulated temperatures ($T_{sim,\ cs}$) obtained from CFD of the drying chamber. As shown, the ($E_r(\%)$) for the three sensors installed in the drying chamber is below 5%.

Based on the results and errors obtained in this research, the CFD model is acceptable. This is because previous research by some authors has conducted experimental and simulation studies, obtaining errors with deviations of 6.5%, 5.34%, and 10% (Afshari *et al*., 2021) (Das *et al*., 2021) (Güler *et al*., 2020); even with an average error of 3.0 % (Elakrout *et al*., 2025).

Some differences between the experimental and simulated values can be attributed to factors such as the limitations of the steady-state model, which does not account for heat accumulation over time, or calibration errors in the thermocouples. Despite these limitations, the overall agreement between the two datasets validates the CFD model as a reliable tool for predicting the thermal behavior of the solar dryer. This has been demonstrated in recent research, where computational simulations were performed in drying chambers under different conditions to evaluate their performance as a function of temperature and air velocity (Rahmat *et al*., 2025).

3.4 Design proposal

Once the model was validated, the drying chamber height (L_{ch}) was adjusted to increase the chamber temperature. For this, the same CFD model of the dryer was used, with the same boundary conditions established in the methodology.

As a computational modeling strategy, data for 1:30 p.m. were considered, accounting for the proposed modifications to the chamber height (L_{ch}) of 100, 80, and 50 cm. The results are shown in Table 6, which demonstrates that as the height of the drying chamber decreases, the increase in internal temperature is greater. Therefore, the ideal chamber height is 50 cm, with a temperature difference of 14 K relative to the original height of the drying chamber.

Subsequently, dryer simulations were repeated for a drying height of 50 cm between 9:30 and 13:30 h. Table 7 shows the simulated versus experimental pipe temperatures. The results have been effective, as comparing the simulated actual size ($T_{sim,\ tub}$) with the simulation at a drying height of 50 cm ($T_{sim,tub,50cm}$) yields a minimum temperature increase (ΔT) of 10.26 K and a maximum of 15.62 K.

On the other hand, the average temperature inside the chamber is shown in Table 8. At 9:30 a.m., the temperature was 330.13 K, an increase of 11.37 K. At 11:30 a.m., the temperature was 323.71 K, an increase of 8.53 K. Finally, at 1:30 p.m., the temperature reached 341.56 K, an increase of 13.43 K. All these values are compared to the simulation of the original system. The 11:30 a.m. temperature is lower than the 9:30 a.m. and 1:30 p.m. temperatures, likely due to higher airflow. However, the results shown in Tables 6 and 7 indicate that the CFD computational model remains promising for predicting temperature distributions and optimizing the performance of thermal systems, thereby reducing the need for physical prototypes, as in this study of the indirect forced-flow solar dryer. Furthermore, according to the results obtained with the new proposal, the temperatures are ideal for this equipment, and it would perform better in the drying process under real-world operating conditions. Therefore, it is promising, as drying fruits, vegetables, and meats requires temperatures between 30 and 70 °C (Tlatelpa-Becerro *et al*., 2019).

Table 7. Comparison of pipe temperatures between experimental and simulated tests.

No. thermocouple	Time (h)	$T_{exp,tub}$ (K)	$T_{sim,tub}$ (K)	$T_{sim,tub,50cm}$ (K)	ΔT (K)
	09:30	301.65	307.98	318.24	10.26
1	11:30	308.15	307.07	318.25	11.18
	13:30	310.90	316.87	329.55	12.68
	09:30	311.90	318.38	332.47	14.10
2	11:30	326.15	316.95	328.61	11.66
	13:30	330.15	326.25	341.88	15.63
	09:30	311.40	318.23	332.24	14.01
3	11:30	325.15	316.84	329.60	12.76
	13:30	330.90	326.01	341.63	15.62
	09:30	311.15	319.33	332.88	13.55
4	11:30	325.15	317.83	330.25	12.42
	13:30	328.15	327.01	343.06	16.05
	09:30	306.15	321.40	330.13	8.73
5	11:30	321.65	314.20	329.66	15.46
	13:30	325.40	328.47	346.33	17.86
	09:30	310.40	318.72	333.68	14.96
6	11:30	325.40	317.21	327.82	10.61
	13:30	331.40	326.08	341.67	15.59
	09:30	313.90	319.58	334.44	14.86
7	11:30	330.15	317.78	328.74	10.96
	13:30	337.40	327.42	342.68	15.26

Table 8. Comparison of the experimental temperature versus the simulated temperature in sensor 1 of the drying chamber.

Time (h)	($T_{exp,cs}$) (K)	($T_{sim,cs}$) (K)	$T_{sim,cs}$ 50 cm (K)	ΔT (K)
09:30	305.55	318.76	330.13	11.37
11:30	315.32	315.18	323.71	08.53
13:30	319.45	328.13	341.56	13.43

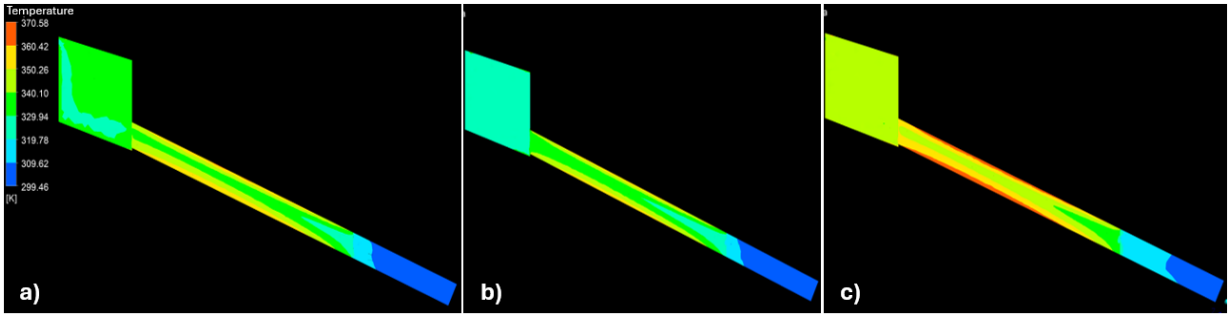

Figure 6. Temperature behavior in the solar dryer, at the times of a) 9:30 a.m., b) 11:30 a.m., and c) 1:30 p.m.

Moreover, these systems remain attractive due to their affordability and ease of maintenance and operation, compared to those powered by non-renewable energy sources. In addition, CFD has been a valuable tool for qualitatively visualizing results for analysis (Figure 6).

Conclusions

Computational fluid dynamics (CFD) analysis was applied to an indirect forced-flow solar dryer, demonstrating its reliability for predicting the thermal behavior of such a dryer. The comparison between experimental data and simulation results shows relative percentage errors of less than 5%, validating the model's accuracy.

Calculations of mass flow rate, Reynolds number, Nusselt number, and convective coefficient confirmed that the flow in the solar collector is turbulent, justifying the use of the RNG k-ε model. Furthermore, the calculated heat transfer rate was consistent with the simulated results, also validating the model.

The simulations predict that reducing the drying chamber height to 50 cm increases the average internal temperature by up to 14 K compared to the original design. Based on this finding, it is expected that drying efficiency will improve and operating time will be reduced without requiring complex structural modifications. However, this chamber height is suitable for products with higher moisture content that require higher temperatures to facilitate moisture removal. Conversely, a drying chamber with a height of 80 cm can be used for products that require lower temperatures, allowing the drying of larger quantities at once.

The design of the solar dryer remains innovative, as it has successfully dried a range of products, including vegetables, fruits, and meats. However, improvements are needed to guarantee drying times and the final quality of the product. Therefore, future work is required, including a study of product loading, changes to the internal configuration of the solar collector, and transient-state analysis to optimize the system using CFD. This approach allows evaluating improvements without building multiple physical prototypes, providing a technical and economic advantage for the development of sustainable food-drying technologies.

References

Afshari, F., Tuncer, A. D., Sözen, A., Ciftci, E., & khanlari, A. (2021). Experimental and numerical analysis of a compact indirect solar dehumidification system. *Solar Energy, 226*, 72-84. doi:10.1016/j.solener.2021.08.025

Benhamza, A., Boubekri, A., Atia, A., Habidi, T., & Arici, M. (2021). Drying uniformity analysis of an indirect solar dryer based on computational fluid dynamics and image processing. *Sustainable energy technologies and assessments, 47*. doi:10.1016/j.seta.2021.101466

Bird, R. B., Stewart, W. E., & Lightfoot, E. N. (2006). *Fenómenos de transporte.* México: Limusa Wiley.Castañeda Magadán, E. O. (2017). Control e instrumentación de un intercambiador de calor experimental.

Cengel, Y. A., & Ghajar, A. J. (2011). *Transferencia de calor y masa. Fundamentos y aplicaciones.* McGraw Hill.

Cetina-Quiñoñnes, A., López-López, J., Ricalde-Cab, L., El Mekaoui, A., San-Pedro, L., & Bassam, A. (2021, 08). Experimental evaluation of an indirect type solar dryer for agricultural use in rural communities: Relative humidity comparative study under winter season in tropical climate with sensible heat storage material. *Solar Energy, 224*, 58-75. doi:10.1016/J.SOLENER.2021.05.040

Das, M., Alic, E., & Akpinar, E. (2021). Numerical and experimental analysis of heat and mass transfer in the drying process of the solar drying system. *Engineering science and technology, an International Journal, 24*(1), 236-246. doi:10.1016/j.jestch.2020.10.003

Demissie, P., Hayelom, M., Kassaye, A., Hailesilassie, A., Gebrehiwot, M., & Venierschot, M. (2019). Design, development and CFD modeling of indirect solar food dryer. *Energy procedia, 158*, 1128-1134. doi:10.1016/j.egypro.2019.01.278

Doymaz, Í., & Ísmail, O. (2011, 01). Drying characteristics of sweet cherry. *Food and Bioproducts Processing, 89*(1), 31-38. doi:10.1016/J.FBP.2010.03.006

Dufera, L., Hofacker, W., Esper, A., & Hensel, O. (2021). Physicochemical quality of twin layer solar tunnel dried tomato slices. *Heliyon, 7*(5). doi:10.1016/j.heliyon.2021.e07127

Elakrout, O., Ghriss, O., Bouabidi, A., & Vanierschot, M. (2025). Experimental and Numerical Investigation of a Novel Low-Cost Solar Air Heater with Large-Scale V-Shaped Fins to Enhance Heat Transfer. *Energies*, *18*(20), 5503. https://doi.org/10.3390/en18205503

Figueroa-García, E., Segura-Castruita, M., Luna-Olea, F., Vázquez-Vuelvas, O., & Chávez-Rodríguez, A. (2021). Design of a hybrid solar collector with a flat plate solar collector and induction heating:. *Revista Mexicana de Ingeniería Química, 20*(3). doi: 10.24275/rmiq/Alim2452

Galindo Luna, J. A., García Castrejón, J. C., Castro Gómez, L. L., & Urquiza Beltrán, G. (2017). Mechanical power variation in hydraulic microturbine regarding the number of blades. *DYNA: Ingeniería e Industria, 92*, 503-506.

García-Moreira, D. P., Pacheco, N., Hernández-Guzmán, H., Bahammou, Y., Tagnamas, Z., Moreno, I., & López-Vidaña, E. C. (2024).

Evaluation of various drying methods for mexican yahualica chili: Drying characteristics and quality assessment. *Advanced Drying Technologies in Food Processing, 12*(9), 1969. doi:10.3390/pr12091969

García-Moreira, D., De Zacatecas, U. A., Moreno, I., Delgadillo-Ruiz, L., & López-Vidaña, E. (2025). Impact of modulation of solar irradiance on spinach drying and its effects on bioactive compounds and quality. *Revista Mexicana de Ingeniería Química*, *24*(3), 1-17. https://doi.org/10.24275/rmiq/alim25628

Getahun, E., Delele, M. A., Gabbiye, N., Fanta, S. W., Demissie, P., & Vanierschot, M. (2021). Importance of integrated CFD and product quality modeling of solar dryers for fruits and vegetables: A review. *Solar energy, 220*, 88-110. doi:10.1016/j.solener.2021.03.049

Gobierno de México. (2016, 09 06). *México Megadiverso*. Retrieved from Gobierno de México: https://www.gob.mx/conanp/es/articulos/mexico-megadiverso-173682?idiom=es.

Güler, H. Ö., Sözen, A., Tuncer, A. D., Afshari, F., Khanlari, A., Sirin, C., & Gungor, A. (2020). Experimental and CFD survey of indirect solar dryer modified with low-cost iron mesh. *Solar energy, 197*, 371-384. doi:10.1016/j.solener.2020.01.021

Iranmanesh, M., Hadi, S. A., & Saleh, B. J. (2020). CFD modeling and evaluation the performance of a solar cabinet dryer equipped with evacuated tube solar collector and thermal storage. *Renewable energy, 145*, 1192-1213.

Kebede, A. Y., Tigabu, M. T., Admase, A. T., & Bezie, A. J. (2024b). Performance evaluation of diminutive solar dryer for drying of green coffee beans: In Ethiopian highlands. *Case Studies In Thermal Engineering*, *65*, 105653. https://doi.org/10.1016/j.csite.2024.105653

Limón Portillo, A. (2017, 06 02). *Energía solar en México: su potencial y aprovechamiento*. Retrieved from Centro de Investigación Económica y Presupuestaria: https://ciep.mx/energia-solar-en-mexico-su-potencial-y-aprovechamiento/

Rahmat, M. A. A., Ibrahim, A., Ishak, M. A. A., Mustaffa, M. U. S., & Al-Aribe, K. M. (2025b). Numerical investigation of thermal and airflow profiles in diverse solar dryer chamber configurations. *Case Studies In Thermal Engineering*, *73*, 106612. https://doi.org/10.1016/j.csite.2025.106612

Romero, V., Cerezo, E., García, M., & Sánchez, M. (2014). Simulation and validation of vanilla drying process in an indirect solar dryer prototype using cfd fluent program. *Energy procedia, 57*, 1651-1658. doi:10.1016/j.egypro.2014.10.156

Tegenaw, P. D., Gebrehiwot, M. G., & Vanierschot, M. (2019). On the comparison between computational fluid dynamics (CFD) and lumped capacitance modeling for the simulation of transient heat transfer in solar dryers. *Solar Energy*, *184*, 417-425. https://doi.org/10.1016/j.solener.2019.04.024

Tlatelpa-Becerro, A., Rico-Martínez, R., Urquiza-Beltrán, G., & Calderón-Ramírez, M. (2019). Obtaining of Crataegus mexicana leaflets using an indirect solar dryer. *Revista Mexicana de Ingeniería Química*, *19*(2), 669-676. https://doi.org/10.24275/rmiq/alim896

Xamán, J., & Gijón-Rievera, M. (2016). *dinámica de fluidos computacionales para ingenieros.* Palilibro.Zukauskas, A. (1972). Heat transfer from tubes in crossflow. *Advances in heat transfer, 8*, 93-160. doi: 10.1016/S0065-2717(08)70038-8